【网络优先出版,实际出版页码及内容以正式版为准】

引用格式: LIU Guoke, WANG Jun, DAI Yunteng, et al. Research on Fiber Optic Fabry-Perot Temperature and Pressure Dual Parameter Sensor Based on MEMS Technology[J]. Acta Photonica Sinica, 2026, 55(7):0706002
刘国柯,王军,戴云腾,等. 基于MEMS技术的光纤法珀温压双参量传感器研究[J]. 光子学报,2026,55(7):0706002

基于MEMS技术的光纤法珀温压双参量传感器研究

刘国柯,王军,戴云腾,刘佳,任乾钰,贾平岗

(中北大学 宽禁带半导体超越照明材料与技术全国重点实验室, 太原 030051)

摘　要:本文提出了一种利用硅敏感膜片进行温压一体测量的光纤法珀传感器,旨在实现高温环境下温度与压力的同点位测量。利用微机电系统技术实现敏感单元的批量化制备,其中,在硅敏感膜片内部设计了凸台结构,压力引发硅膜片的弹性微形变,温度则导致膜片-凸台一体结构产生热致形变。结合互相关解调技术进行温度解耦,有效减少了温度对压力测量的交叉干扰,提高了高温环境下压力的测量精度。实验结果表明,在0~500 kPa的压力范围内,传感器的非线性误差为0.17% F.S,迟滞误差为0.62% F.S,重复性误差为0.72% F.S。在350 ℃高温环境下,温度测量精度为0.21% F.S。经过温度补偿后,传感器的压力测量精度提高至1.17% F.S。此外,传感器具有高一致性、全无胶化集成、抗电磁干扰等优点。该研究为高温环境下温度和压力同步测量提供了一种新的思路,在高温高压领域具有广泛的应用前景。

关键词:光纤传感器;法布里-珀罗;微机电系统;温压测量;高温
中图分类号:TP212　　**文献标识码**:A　　**doi**:10.3788/gzxb20265507.0706002

0 引言

高温压力测量在航空发动机、燃气轮机等高端装备的热端部件性能评估中具有重要意义[1-2],燃烧室后段和石油工业等高温部位的压力场分布直接影响整机的运行效率、可靠性及寿命预测[3-5]。因此,准确可靠的高温压力测量技术对于提升装备性能和保障运行安全至关重要。目前,现有的高温压力传感器主要依赖压电式[6-7]、SOI压阻式[8]和陶瓷电容式[9-10]等电学传感器,尽管其在一定条件下可提供较为准确的测量结果,但在复杂电磁干扰环境下,电学传感器的核心敏感元件易受热-力-电多场耦合作用的影响,导致长期稳定性差,从而限制了其在高温环境下压力测量的可靠性和准确性。

与电学传感器相比,光纤传感器凭借抗腐蚀、无源、抗电磁干扰、耐高温及微型化等优势,在高温高压测量中展现出巨大潜力[11-13]。MA Weiyi等[14]采用硼-硅玻璃阳极键合工艺,通过优化膜片半径与厚度研制出一种高精度法布里-珀罗(Fabry-Perot,F-P)压力传感器,但其低温漂特性仅适用于常温~70 ℃。DUAN Bowen等[15]提出了一种基于三层蓝宝石直接键合技术制备的光纤F-P压力传感器,实现20~370 ℃范围内的压力测量,但受温漂影响且未引入温度补偿,导致测量误差超过2%。李加顺等[16]采用三层石英键合工艺制作的全石英压力传感器,将工作温度提升至800 ℃,尽管全石英结构减小了热膨胀的影响,但在整个温度区间内仍存在温压交叉干扰。由于压力敏感膜片的力学参数受温度影响,普通光纤传感器的热致腔长漂移问题愈发显著[17],温压交叉敏感问题成为高温精准测量的主要瓶颈。因此,对高温压力进行温度解耦,有利于进一步提升传感器测量精度。

基金项目:国家自然科学基金(52505617)
第一作者:刘国柯(1999—),男,硕士,主要研究方向为光纤法珀压力传感器。Email: liuguoke112@163.com
通讯作者:贾平岗(1982—),男,教授,博士,主要研究方向为高温光纤传感器技术与系统。Email: pgjia@nuc.edu.cn
收稿日期:2026-02-05;**录用日期**:2026-04-20

高温环境下温压双参测量是实现压力温度解耦、提升测量精度的重要手段。LIU Yinggang等[18]级联光纤布拉格光栅(Fiber Bragg Grating,FBG)与法布里-珀罗干涉仪(Fabry-Perot Interferometer,FPI),利用FPI对温压的敏感和FBG对温度的单一响应,实现30～110 ℃、0.1～0.7 MPa的双参量测量,但该结构难以批量生产。JIA Pinggang等[19]结合微机电系统(Micro-Electro-Mechanical System,MEMS)技术和CO_2激光焊接工艺,将FBG与阳极键合硅敏感单元集成,实现了20～350 ℃、0～0.5 MPa的双参量同步测量,且一致性高、可批量化生产。另一种方法是利用F-P腔进行测温,王昊星等[20]设计了一种基于金属膜片的光纤高温压力传感器,通过金属膜片的形变测压,并利用蓝宝石背板F-P腔的热膨胀特性测温。类似的,LIU Jia等[21]采用MgO背板F-P腔实现温度响应。然而,对于引入FBG或背板等额外结构响应温度变化,由于温度与压力感知结构存在物理分离,难以保证二者处于同一温度区域,从而限制了同点位温度补偿的精度。

本文提出了一种基于MEMS技术的光纤法珀温压双参量传感器。设计了带有凸台的硅敏感膜片,经理论分析和仿真优化结构参数;利用MEMS技术批量化制备,采用CO_2激光焊接实现传感器全固态无胶化集成,结合互相关解调技术,在不引入额外温度感知单元下,根据敏感膜片在复合环境下形变实现温压双参量的同点位测量,为提升高温压力测量精度提供了一种具有广泛应用前景的解决方案。

1　传感器设计原理及仿真

1.1　传感器结构设计与原理

该传感器主要由耐高温敏感单元、中空玻璃毛细管和聚酰亚胺单模光纤组成,其结构示意图如图1所示。光纤端面切平处理后,插入中空玻璃毛细管内,利用CO_2激光焊接将聚酰亚胺单模光纤与玻璃毛细管集成,随后将玻璃管插入基座,确保光纤端面与单晶硅敏感膜片内部凸台精确对准,从而形成第一个微型法布里-珀罗干涉腔(FP1),用于外部压力的测量。同时,硅敏感膜片的外部感压面与内部凸台端面之间形成第二个法布里-珀罗干涉腔(FP2),用于温度测量。

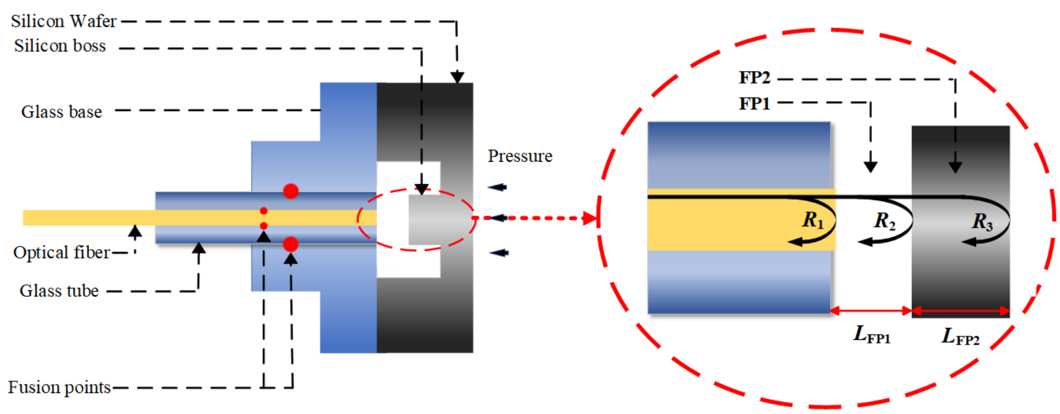

图1　传感器的结构示意图

Fig. 1　Schematic diagram of the sensor

在温压复合环境下,外部压力作用于硅敏感膜片,导致其发生微变形,从而引起FP1腔长L_{FP1}变化。与此同时,外界温度的变化使硅敏感膜片发生热膨胀,导致FP2腔长L_{FP2}变化。L_{FP1}和L_{FP2}同时受硅敏感单元膜片的影响,这两种物理效应共同调制干涉光谱的相位,并通过光纤将调制后的光信号传输至远端光谱解调仪,实现对温度与压力双参量的实时监测。

为提高测量精度,在硅敏感单元内部设计并刻蚀了凸台结构。该凸台的引入使得当敏感膜片受到外部压力作用时,膜片内表面趋向于平行形变,有效减小了因膜片弧形变形引起的F-P腔两端面平行度急剧变差所产生的测试误差。当入射光通过光纤进入传感器的敏感单元后,先经过切平的光纤端面,然后到达敏感膜片凸台表面,光透射过凸台表面后最终抵达感压端面,在这个过程中,光在三个反射面之间发生多次干涉,如图1所示。根据多光束干涉原理,反射光强I_r与入射光强I_i之间的关系可以表示为[22]:

$$I_r=\left[R_1+R_2+R_3+2\sqrt{R_1R_2}\cos(4\pi n_1L_{FP1}/\lambda)+2\sqrt{R_2R_3}\cos(4\pi n_2L_{FP2}/\lambda)+2\sqrt{R_1R_3}\cos\left[(4\pi n_1L_{FP1}/\lambda)+(4\pi n_2L_{FP2}/\lambda)\right]\right]I_i \tag{1}$$

式中，R_1、R_2和R_3为三个反射面的反射率，n_1和n_2分别是FP1和FP2介质的折射率，λ为入射光波长。由式(1)可得，当传感器敏感单元结构与材料确定后，传感器光谱输出与L_{FP1}和L_{FP2}有关。因此，在设计敏感单元前需要进行理论分析。根据小挠度理论可知，当外界施加均匀分布的压力P时，平面硅敏感膜片将发生形变，L_{FP1}相应减小，在压力作用下圆形膜片的中心偏移量ω_0为[23]：

$$\omega_0=\frac{3P(1-\mu^2)}{16Eh^3}r^4 \tag{2}$$

式中，P为施加在硅敏感膜片上的压力；E为杨氏模量；μ为泊松比；r为膜片的有效半径；h为敏感膜片厚度。对于引入凸台的硅敏感膜片，其中心偏移量ω为[24]：

$$\omega=\frac{3P(1-\mu^2)}{16Eh_1^{\ 3}}A_r \tag{3}$$

$$A_r=r_1^{\ 4}\left(1-\frac{r_2^{\ 4}}{r_1^{\ 4}}-4\frac{r_2^{\ 2}}{r_1^{\ 2}}\ln\frac{r_1}{r_2}\right) \tag{4}$$

式中，r_1为膜片的有效半径；h_1为敏感膜片厚度；r_2为凸台半径；传感器灵敏度S可以表示为：

$$S=\frac{\omega_{max}}{P}=\frac{3(1-\mu^2)}{16Eh_1^{\ 3}}A_r \tag{5}$$

根据理论分析可知，传感器的灵敏度S主要取决于敏感单元的尺寸及其材料特性，二者共同决定了传感器在外部激励下的响应特性。考虑到批量化生产对工艺一致性和成本控制的要求，同时兼顾传感器长期稳定性和良好气密性的优势，最终选用单晶硅作为传感器敏感膜片的材料，采用打通孔的高硼硅玻璃作为敏感膜片支撑基座，在满足核心性能指标的同时，亦有利于实现结构简化与工艺集成。

1.2 有限元仿真分析

传感器的敏感膜片是决定其灵敏度、可靠性和其他性能的核心部件。为了评估传感器的性能参数，对传感器敏感膜片尺寸与灵敏度的关系、相同灵敏度的凸台膜片与平膜片在同一压力下峰谷值(Peak-to-Valley Value，PV)的差异进行仿真，PV指的是在一定压力下感压膜片中心约束范围内最大位移与最小位移的差值，如图2所示。

仿真结果表明，传感器的灵敏度、敏感膜片的半径和厚度之间存在相互制约关系。在施加相同压力下，带有凸台的膜片在中心0.2 mm半径范围内的表面位移产生的PV明显小于平膜片，这显著提升了光纤端面与膜片凸台形成的F-P腔的平行度，从而有助于增强传感器出射光干涉信号的对比度，进一步提升了传感

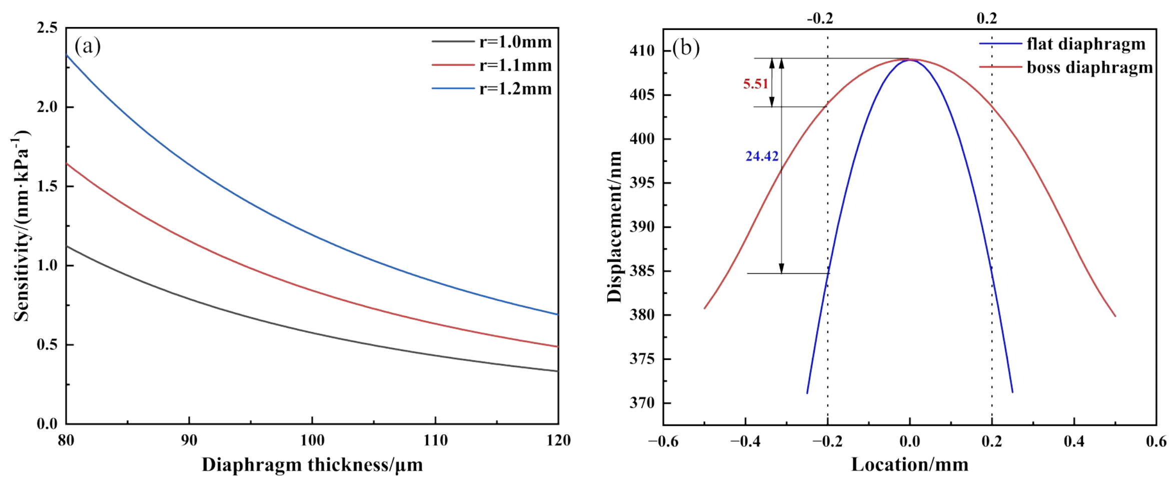

图2 有限元仿真。(a)膜片尺寸与灵敏度关系仿真；(b)相同灵敏度的凸台膜片与平膜片在同一压力下PV的差异

Fig. 2 Finite element simulation. (a) Simulation of the relationship between diaphragm size and sensitivity; (b) Difference in PV between a boss diaphragm and a flat diaphragm with the same sensitivity under the same pressure

器的解调和测试精度。同时,在传感器结构参数的设计过程中,需综合考虑测试需求、工艺可实现性、CO_2激光焊接气密性以及与解调系统的适配等多方面因素。因此,结合理论与实际应用分析,表1中列出了传感器的设计参数。

表1 压力传感器的结构参数

Table 1 Structural parameters of the pressure sensor

Performance	Value
Diaphragm radius r_1/mm	1.1
Diaphragm thickness h_1/μm	100
Boss radius r_2/mm	0.5
Boss thickness h_2/μm	150
Measurement range P/kPa	0－500
Sensitivity S/ (nm•kPa^{-1})	0.85

1.3 互相关解调及温度解耦原理

为了获得压力腔(FP1)和温度腔(FP2)的数据,在上位机采集到实际光谱数据后,需通过软件互相关解调算法对其进行处理。互相关解调通过计算实际光谱数据向量与不同腔长的虚拟光谱数据向量之间的互相关函数,获取互相关系数。当互相关系数取得最大值时,表明两向量之间的相关性达到最强,此时选取与实测光谱数据最匹配的理论光谱数据所对应的腔长,作为传感器腔长的最终解调结果。在此过程中,光频率为f,光在真空中的传播速度为c,根据式(1),传感器的频域干涉光谱可表示为:

$$R_{FP}(f)=A+B_1\cos\left(\frac{4\pi n_1 L_{FP1}}{c}f\right)+B_2\cos\left(\frac{4\pi n_2 L_{FP2}}{c}f\right)+B_3\cos\left(\frac{4\pi n_1 L_{FP1}}{c}f+\frac{4\pi n_2 L_{FP2}}{c}f\right) \tag{6}$$

式中$A=R_1+R_2+R_3$、$B_1=2\sqrt{R_1R_2}$、$B_2=2\sqrt{R_2R_3}$、$B_3=2\sqrt{R_1R_3}$。将光谱信号通过快速傅里叶变换(FFT)转换至频域,得到相应的频谱。根据FP1与FP2干涉信号各自对应的中心频率,分别确定带通滤波器的系数,对频谱进行滤波处理,再对滤波后的频谱进行快速傅里叶逆变换(IFFT),即可分离出FP1和FP2所对应的干涉信号。通过建立温度T_i、传感器压力腔长L_{FP1}、传感器温度腔长L_{FP2}、灵敏度S之间的关系进行温度解耦,即:

$$\begin{cases}T(L_{FP2})=T_i\\L(T_i)=L_0\\L_{FP1}=L_0-S_iP_{meas}\end{cases} \tag{7}$$

$$P_{meas}=-\frac{L_{FP1}-L_0}{S_i} \tag{8}$$

其中,L_0为不同温度下FP1的初始值,S_i为不同温度下传感器的灵敏度,解耦后的压力值为P_{meas}。

2 传感器制造集成

传感器的关键结构采用了MEMS技术、硅-玻璃阳极键合和CO_2激光焊接技术进行封装与集成,利用MEMS技术实现微型化、批量化生产敏感单元,而阳极键合通过静电作用形成无中间层的全固态密封,具备优异的气密性和与硅相匹配的热膨胀系数,且不含任何有机材料,保障了敏感单元的长期可靠封装,最终使用激光焊接技术进行集成组装,消除了异质材料的引入,有效地抑制了高温环境中的热失配问题。三者结合形成了一种全固态、无有机粘合剂的密封结构。此设计显著提高了传感器在高温、高压等工况下的长期结构完整性和测量稳定性。

敏感单元的MEMS制造工艺主要包括单晶硅片的刻蚀、硅-玻璃阳极键合和敏感单元与光纤的集成。详细的工艺流程如图3所示。

首先,选取厚度为300 μm的双面抛光单晶硅片,经标准RCA清洗去除表面污染物后,采用旋涂法均匀涂覆正性光刻胶,并进行前烘。通过光刻与显影工艺,形成直径2.2 mm的圆形掩膜图形。随后,在120 ℃下坚膜20 min以增强胶膜附着力,采用感应耦合等离子体深硅刻蚀技术,以光刻胶为掩模,进行各向异性刻

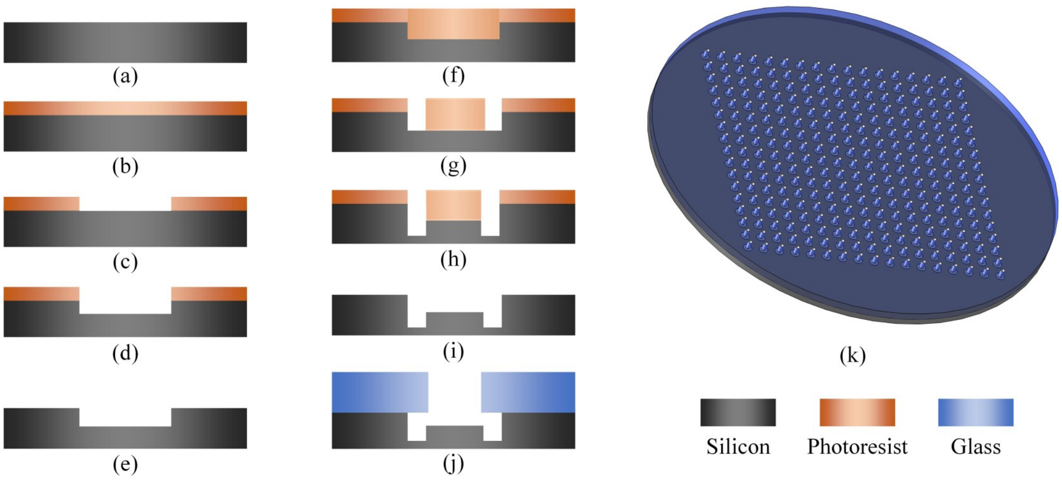

图3　硅敏感单元制备工艺流程图。(a)硅片;(b)匀胶;(c)光刻显影;(d)刻蚀硅;(e)去除光刻胶;(f)二次匀胶;(g)二次光刻显影;(h)二次刻蚀硅;(i)二次去除光刻胶;(j)阳极键合;(k)未切割的晶圆

Fig. 3　Process flow diagram for fabrication of silicon sensing element. (a) Silicon wafer; (b) Uniform Photoresist; (c) Photolithography and development; (d) Silicon etching; (e) Remove photoresist; (f) Second uniform photoresist; (g) Second photolithography and development; (h) Second silicon etching; (i) Second remove photoresist; (j) Anodic bonding; (k) Unsegmented wafer

蚀,精确去除50 μm厚硅材料,形成厚度为250 μm的圆形敏感膜片。之后,使用丙酮超声剥离并彻底去除残留光刻胶,如图3(a)～(e)所示。接下来,进行第二次光刻与深硅刻蚀,工艺过程与前者类似,此次刻蚀区域为内径1 mm、外径2.2 mm的环形区域,刻蚀深度为150 μm,从而在敏感膜片中央形成高度为150 μm、直径1 mm的硅凸台结构,至此形成刻蚀深度为200 μm的圆环,厚度为100 μm的敏感膜片,如图3(f)～(i)所示。最后,将制备好的硅微结构单元与预先加工有对应通孔的双面抛光BF33高硼硅玻璃在高温高压下进行阳极键合,实现硅-玻璃间的密封结合。最终,在4英寸晶圆上形成17×17的传感器敏感单元阵列,如图3(j)～(k)所示。

利用计算机数控(Computer Numerical Control,CNC)技术将阳极键合的晶圆切割并分离为边长为4 mm的正方形敏感单元,切割公差控制在±5 μm以内,以确保阳极键合区域具有足够的键合面积,降低因键合面积不足而引发漏气的风险,硅晶圆与玻璃基座键合部分的单侧最小尺寸约为1.8 mm,键合面积约为12.2 mm^2,该键合面积在本课题组多项研究工作中已经验证[16,25]。敏感单元键合与切割分离示意图如图4(a)和(b)所示,实物图如图4(d)和(e)所示。随后,采用CO_2激光器对端面切割平整的单模光纤与毛细玻璃管进行熔融焊接。焊接完成后,将光纤经过通孔插入敏感单元内部,并观察反射光谱。当光谱质量达到理想状态时,利用CO_2激光器完成敏感单元与毛细玻璃管的焊接密封集成,制备后的传感器如图4(c)和(f)所示。

3　测试与分析

为了验证传感器在温度-压力环境中的性能,通过搭建温度-压力复合环境联合测试平台,对所研制的光纤F-P传感器在常温～350 ℃范围内的压力响应进行了测试,测试系统如图5所示。该实验系统主要由传感器、光谱解调器、上位机、真空温压复合炉(JT1500)以及氩气瓶等关键组件构成,最高额定温度为1500 ℃,通过控制钽加热器实现温度控制,控制精度为±1 ℃,最大可供给1 MPa压力,精度为±0.1 kPa。在实验过程中,总控机负责控制温压复合炉的升温过程及保温时间,同时监控并控制炉内压力的供给。传感器被固定于真空温压炉内,并通过侧壁密封法兰与外部光谱解调仪连接,以确保光信号的有效传输。上位机实时记录解调仪输出的干涉光谱数据,从而全面评估传感器在温压复合环境下的响应特性。

将传感器安装于温压复合炉内后,上位机采集的反射光谱如图6(a)所示,对频谱进行傅里叶变换,得到两个特定的干扰信号,图6(b)和(c)分别显示了L_{FP1}和L_{FP2}的互相关结果,此时L_{FP1}=239.721 μm,L_{FP2}=882.645 μm。常温压力性能实验的初始压强设定为0,以100 kPa的步长逐级增压至500 kPa。每个压力点

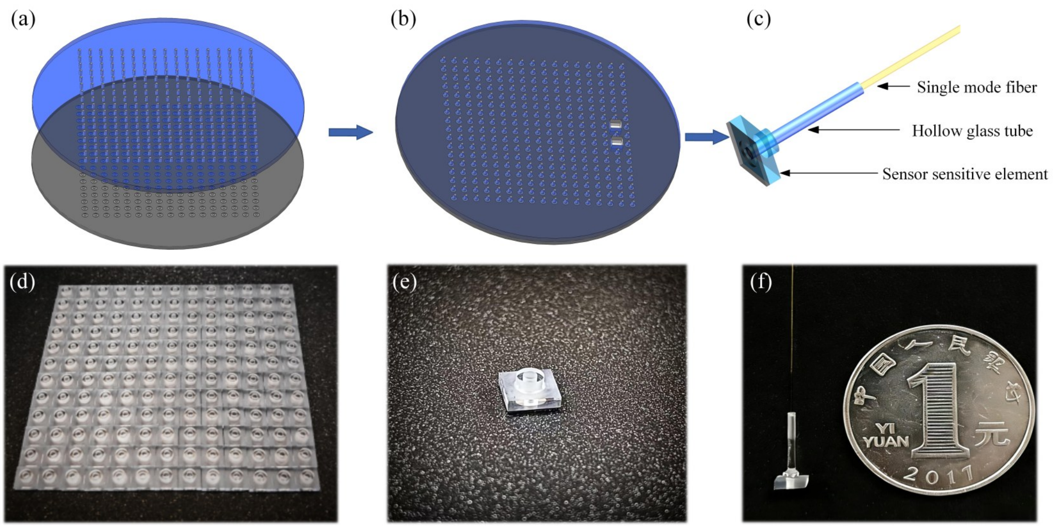

图4 传感器敏感单元与光纤集成。(a)阳极键合示意图;(b)敏感单元切割示意图;(c)传感器集成示意图;(d)敏感单元切割阵列;(e)单一敏感单元;(f)传感器集成实物图

Fig. 4 Integration of sensor sensing element with fiber optic. (a) Schematic diagram of anodic bonding; (b) Schematic diagram of sensing element cutting; (c) Schematic diagram of sensor integration; (d) Array of cut sensing elements; (e) Single sensing element; (f) Photograph of the integrated sensor

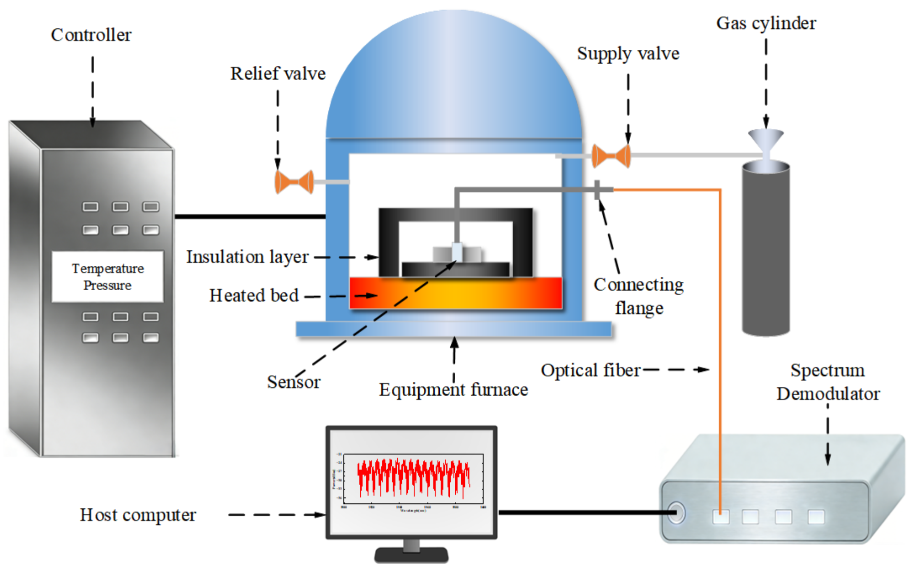

图5 传感器温度-压力复合测试系统示意图

Fig. 5 Schematic diagram of sensor Temperature-Pressure combined test system

保持恒定2分钟,以确保腔长数据的稳定采集。压力-腔长L_{FP1}的响应关系如图7(a)所示,对升压过程中的数据进行线性拟合,得到传感器的非线性误差为0.17% F.S,灵敏度为0.83 nm/kPa,接近理论设计值0.85 nm/kPa,其微小偏差主要源于硅敏感膜片刻蚀的平整度和工艺误差。为进一步验证传感器性能,进行了三次相同步长的升降压循环测试,且在每个压力点均保持恒压2分钟并记录腔长,响应曲线如图7(b)所示。分析结果表明,传感器的迟滞为0.62% F.S,重复性误差为0.72% F.S。

由总控机控制从常温开始以50 ℃为步长、10 ℃/min、最高温度350 ℃进行高温实验测试,传感器的温度漂移L_0和L_{FP2}的拟合曲线如图8(a)、8(b)所示,L_0和L_{FP2}均随温度升高而增大。其中,初始腔长L_0主要受空气热膨胀的影响,与温度T_i的数学关系如式(9)所示,而L_{FP2}的增大主要由硅材料自身热膨胀引起,对温度更加敏感,与温度T_i呈二次关系,如式(10)所示。

$$L_0 = 239.67247 + 1.92 \times 10^{-3} T_i + 1.38957 \times 10^{-5} T_i^2 - 2.91111 \times 10^{-8} T_i^3 \tag{9}$$

$$L_{FP2} = 880.91439 + 7.438 \times 10^{-2} T_i + 1.42786 \times 10^{-5} T_i^2 \tag{10}$$

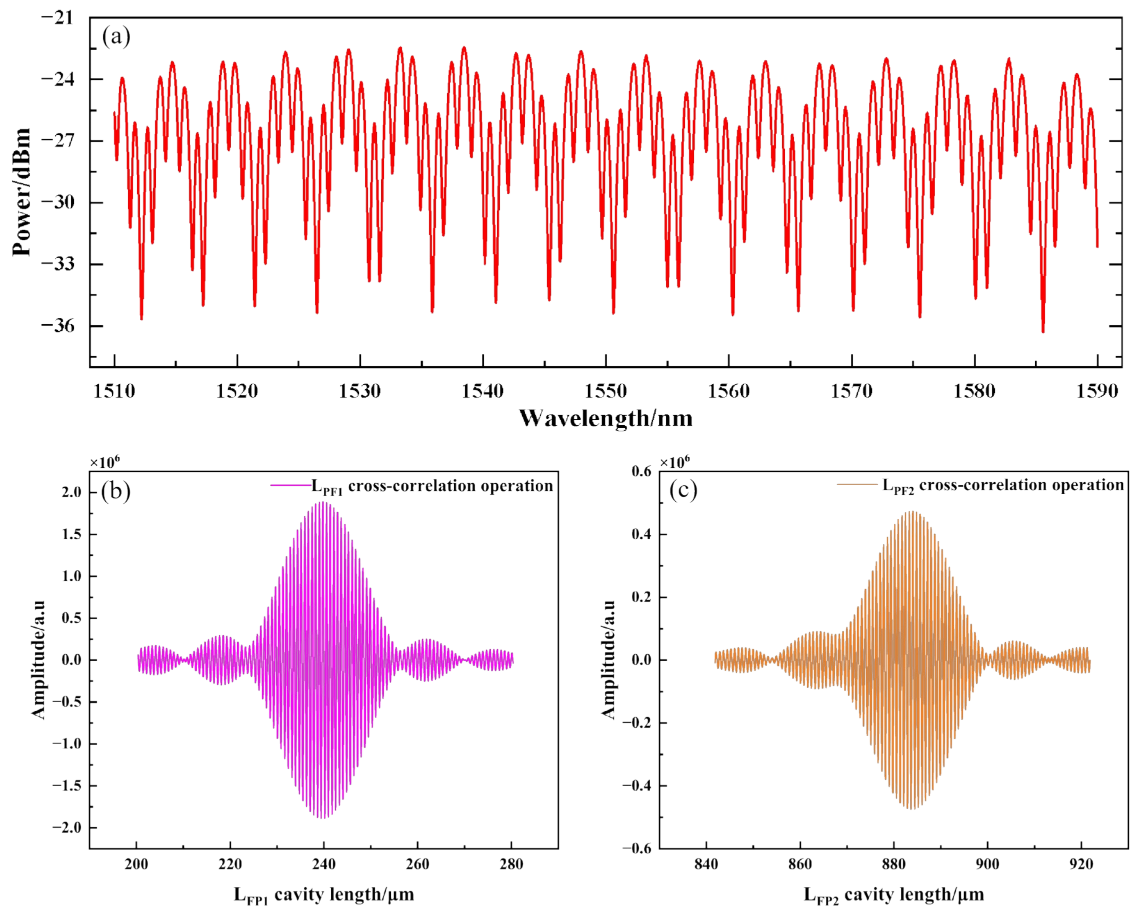

图6　光谱互相关。(a)传感器原始光谱;(b)L_{FP1}的互相关结果;(c)L_{FP2}的互相关结果

Fig. 6　Spectral cross-correlation. (a) Original sensor spectrum; (b) Cross-correlation result of L_{FP1}; (c) Cross-correlation result of L_{FP2}

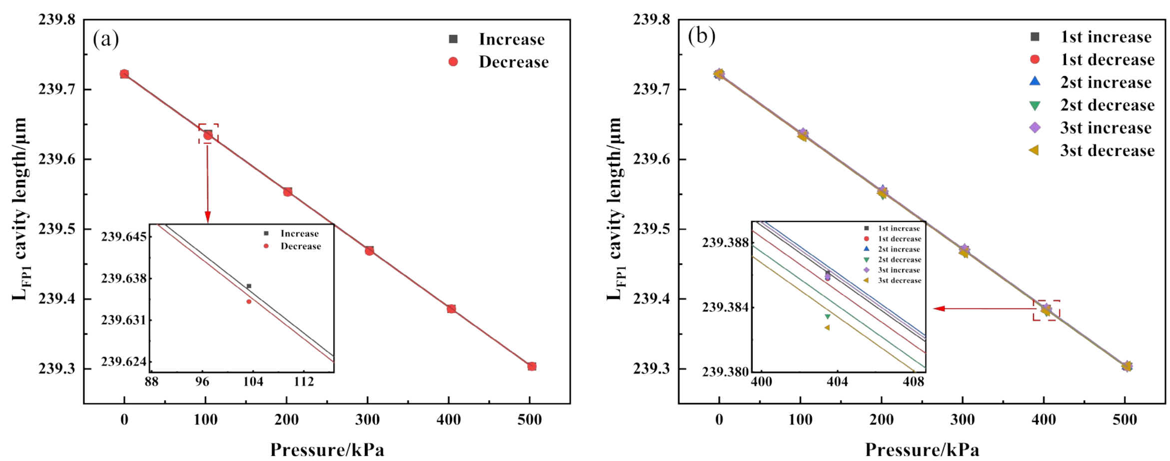

图7　传感器常温下压力响应。(a)常温下升压和降压测试;(b)常温下重复性测试

Fig. 7　Sensor pressure response at room temperature. (a) Pressure increase and decrease test at room temperature; (b) Repeatability test at room temperature

为了验证传感器在高温下的压力响应,在每个温度节点保温30分钟,保证测试环境温度达到设定温度,随后以100 kPa为步长测试传感器在0~500 kPa压力下的响应,如图8(c)所示,实验结果表明传感器在常温~350 ℃温度范围内,最大非线性误差为1.15% F.S,同时,灵敏度随温度的升高而增大,从0.83 nm/kPa升高至1.01 nm/kPa,如图8(d)所示,其与温度的关系符合三次多项式(11)。

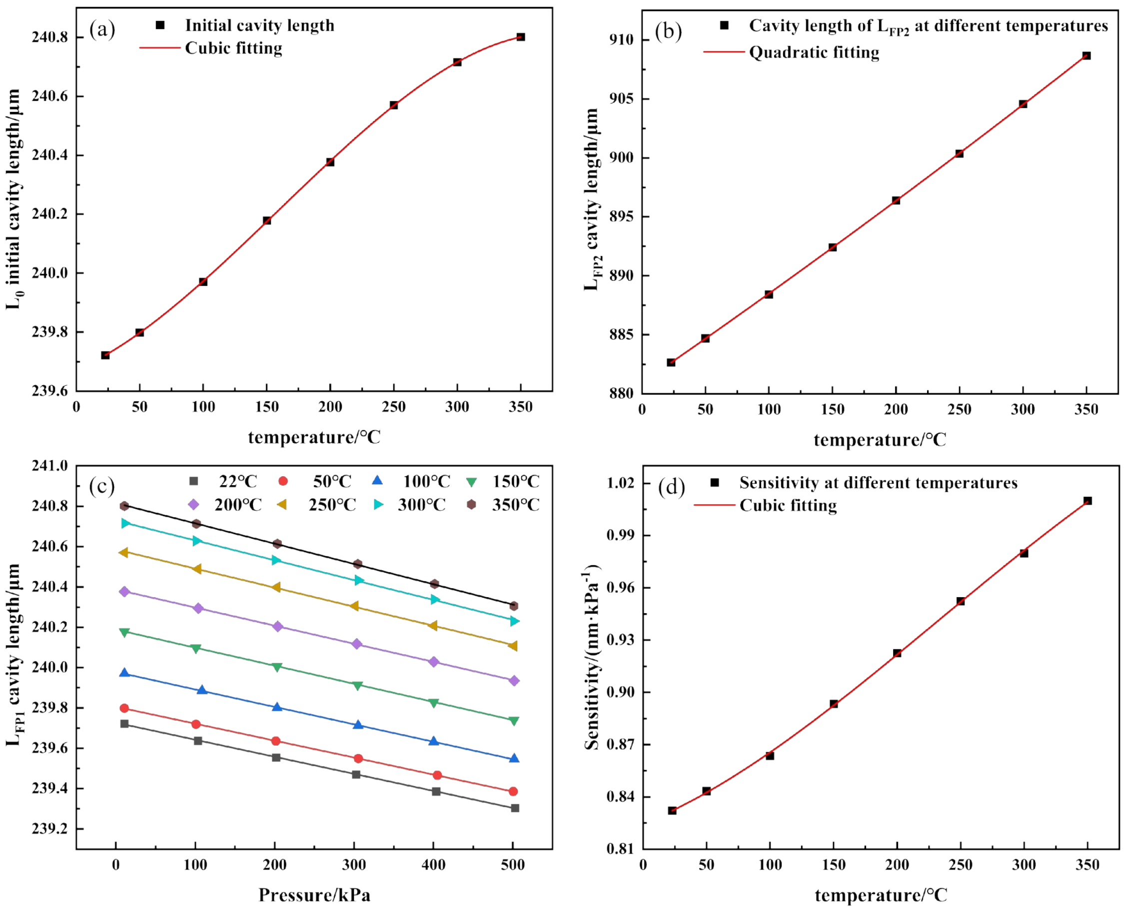

图8　高温压力响应结果。(a)初始腔长L_0与温度的关系；(b)不同温度下L_{FP2}的变化；(c)传感器在常温~350 ℃的压力响应；(d)传感器在常温~350 ℃的灵敏度

Fig. 8　High-temperature pressure response results. (a) Relationship between initial cavity length L_0 and temperature; (b) Changes in L_{FP2} at different temperatures; (c) Pressure response of the sensor from room temperature to 350 ℃; (d) Sensitivity of the sensor from room temperature to 350 ℃

$$S_i = 8.2459\times10^{-4} + 2.9677\times10^{-7}T_i + 1.32095\times10^{-9}{T_i}^2 - 1.888889\times10^{-12}{T_i}^3 \tag{11}$$

$$T_i = -33306.05039 + 62.26268L_{FP2} - 0.02776{L_{FP2}}^2 \tag{12}$$

根据式(10)逆推得到温度T_i与L_{FP2}的数学关系式(12)，在实际测量中，通过上位机采集光谱获得L_{FP2}的数值后，将其代入式(12)可以计算出传感器解耦后的温度值为T_i，得到的T_i分别代入式(9)和(11)，得到传感器在该温度下压力腔的初始值L_0和灵敏度S_i，最后将该温度T_i下各压力点P_i对应的压力室腔长L_{FP1}代入式(8)，即可得到传感器温度解耦后各点对应的压力值P_{meas}。经过高温测试后，各测试温度点解耦温度与炉内实际温度对比如图9(a)所示，常温~350 ℃下解耦后压力与炉内实际压力对比如图9(b)所示。分析实验结果，当温压复合炉温度为350 ℃时，L_{FP2}空腔长度为908.668 μm，得到解耦温度T_i为349.26 ℃，测量偏差为0.74 ℃，测量精度为0.21% F.S；解耦压力P_{meas}与L_{FP1}处各点实际压力P_i对比最大测量偏差为5.83 kPa，测量精度为1.17% F.S。

表2为本文与现有温压双参量传感器性能对比，相比F-P+FBG和其他双F-P等非同位温压双参量测量结构，本文在不引入额外温度感知部件下，利用硅凸台膜片实现温压一体同位测量，该结构可以减小因温度感知结构与压力感知结构异位所造成的温差，提高传感器测量精度。测试结果验证了利用硅敏感膜片进行温压一体同点位测量的可行性和准确性。

4　结论

本文将光纤法珀干涉原理与硅MEMS技术相结合，通过优化传感器敏感单元结构设计，提出了一种基

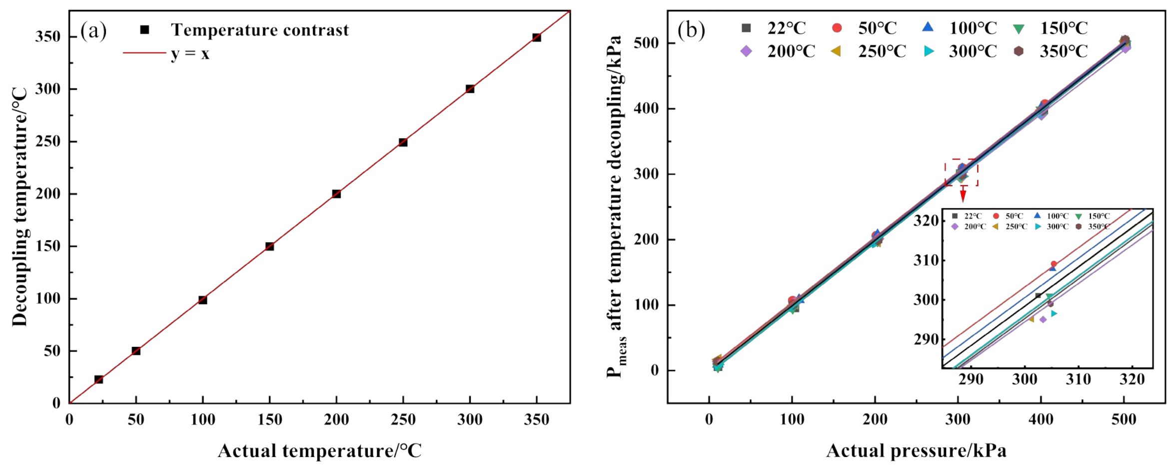

图9 温度解耦结果。(a)解耦温度与实际温度对比;(b)常温～350 ℃解耦压力与实际压力对比

Fig. 9 Temperature decoupling results. (a) Comparison of decoupled temperature with actual temperature; (b) Comparison of decoupled pressure and actual pressure from room temperature to 350 ℃

表2 光纤温压双参量传感器性能对比

Table 2 Performance comparison of fiber-optic temperature-pressure dual-parameter sensors

References	Measurement structure	Co—located measurement	Temperature range	Sensitivity	Temperature accuracy	Pressure accuracy
[18]	F—P+FBG	No	30—110 ℃	0.02 nm/kPa	Not mentioned	Not mentioned
[19]	F—P+FBG	No	20—350 ℃	7.89 nm/kPa	Not mentioned	1.05% F.S
[20]	Dual F—P	No	22—300 ℃	0.47 nm/kPa	1.41% F.S	1.7% F.S
[21]	Dual F—P	No	22—800 ℃	0.27 nm/kPa	1.22% F.S	2.01% F.S
This work	Dual F—P	Yes	22—350 ℃	0.85 nm/kPa	0.21% FS	1.17% F.S

于硅敏感膜片实现温压双参数同点位测量的技术。实验结果表明,该传感器在静态测试中的非线性误差为0.17% F.S,迟滞误差为0.62% F.S,重复性误差为0.72% F.S。经过多参数温度解耦后,传感器在350 ℃高温环境下的温度测量精度为0.21% F.S,压力测量精度为1.17% F.S。该传感器制备过程更为简便且一致性较好,可以实现批量化生产,全固态无胶化集成使其在高温环境下具备良好的气密性和稳定性,为航空航天、高温化工过程等复合环境下的压力监测提供了一种可靠的技术方案,具有广阔的应用前景。

参考文献

[1] CHEN Yankun, XU Qian, ZHANG Xiuqin, et al. Materials and sensing mechanisms for high-temperature pressure sensors: a review[J]. IEEE Sensors Journal, 2023, 23(22): 26910-26924.

[2] LIANG Ting, LI Wangwang, LEI Chen, et al. All-SiC fiber-optic sensor based on direct wafer bonding for high temperature pressure sensing[J]. Photonic Sensors, 2022, 12(2): 130-139.

[3] DENG Yongqiang, JIANG Jin. Optical fiber sensors in extreme temperature and radiation environments: A review[J]. IEEE Sensors Journal, 2022, 22(14): 13811-13834.

[4] LIU Mingyao, WU Yihang, SONG Han, et al. Multiparameter measuring system using fiber optic sensors for hydraulic temperature, pressure and flow monitoring[J]. Measurement, 2022, 190: 110705.

[5] ZHANG Yongtong, JIANG Yi, YANG Shuiwang, et al. All-sapphire fiber-optic sensor for the simultaneous measurement of ultra-high temperature and high pressure[J]. Optics Express, 2024, 32(8): 14826-14836.

[6] KIM N I, YARALI M, MORADNIA M, et al. Piezoelectric sensors operating at very high temperatures and in extreme environments made of flexible ultrawide-bandgap single-crystalline AlN thin films[J]. Advanced Functional Materials,

2023, 33(10): 2212538.

[7] KIM N I, CHANG Yuli, CHEN Jie, et al. Piezoelectric pressure sensor based on flexible gallium nitride thin film for harsh-environment and high-temperature applications[J]. Sensors and Actuators A: Physical, 2020, 305: 111940.

[8] YAO Zong, LIANG Ting, JIA Pinggang, et al. A high-temperature piezoresistive pressure sensor with an integrated signal-conditioning circuit[J]. Sensors, 2016, 16(6): 913.

[9] MA Chao, XIONG Chunyue, ZHAO Rui, et al. Capacitive pressure sensors based on microstructured polymer-derived SiCN ceramics for high-temperature applications[J]. Journal of Colloid and Interface Science, 2025, 678: 503-510.

[10] LI Chen, SUN Boshan, JIA Pengyu, et al. Capacitive pressure sensor with integrated signal-conversion circuit for high-temperature applications[J]. IEEE Access, 2020, 8: 212787-212793.

[11] MA Shaonian, XU Yanping, PANG Yuxi, et al. Optical fiber sensors for high-temperature monitoring: a review[J]. Sensors, 2022, 22(15): 5722.

[12] YU Luyao, ZHAO Qiang, DU Dawei, et al. Diaphragm-type Fiber Bragg Grating Pressure Sensor with a Temperature Compensation Structure[J]. Acta Photonica Sinica. 2022, 51(3): 0306007.
于璐瑶，赵强，杜大伟，等. 膜片式带温补结构的光纤光栅压力传感器[J]. 光子学报，2022，51(3)：0306007.

[13] LIU Tianmu, Jiang Yi, Cui Yang. Photonic Crystal Fiber Temperature and Pressure Sensor[J]. Acta Photonica Sinica. 2020, 49(4): 0406001.
刘天沐，江毅，崔洋. 光子晶体光纤温度压力传感器[J]. 光子学报，2020，49(4)：0406001.

[14] MA Weiyi, JIANG Yi, HU Jie, et al. Microelectromechanical system-based, high-finesse, optical fiber Fabry – Perot interferometric pressure sensors[J]. Sensors and Actuators A: Physical, 2020, 302: 111795.

[15] DUAN Bowen, ZhenyinHAI, GUO Maocheng, et al. A large-range and high-sensitivity fiber-optic Fabry – Perot pressure sensor based on a membrane-hole-base structure[J]. Micromachines, 2024, 15(2): 174.

[16] LI Jiashun, JIA Pinggang, WANG Jun, et al. Silica-MEMS-based Fiber-optic Fabry-Perot Pressure Sensor for High-temperature Applications[J]. Acta Photonica Sinica, 2022, 51(6): 0606005.
李加顺，贾平岗，王军，等. 基于石英MEMS技术的光纤法布里-珀罗高温压力传感器(英文)[J]. 光子学报，2022，51(6)：0606005.

[17] LI Sainan, LIANG Ting, WANG Wei, et al. A novel SOI pressure sensor for high temperature application[J]. Journal of Semiconductors, 2015, 36(1): 014014.

[18] LIU Yinggang, YANG Danqing, WANG Yuxi, et al. Fabrication of dual-parameter fiber-optic sensor by cascading FBG with FPI for simultaneous measurement of temperature and gas pressure[J]. Optics communications, 2019, 443: 166-171.

[19] JIA Pinggang, LIANG Hao, FANG Guocheng, et al. Batch-producible MEMS fiber-optic Fabry-Perot pressure sensor for high-temperature application[J]. Applied Optics, 2018, 57(23): 6687-6692.

[20] WANG Haoxing, LIU Jia, WANG Haiyang, et al. Metal-sensitive diaphragm fiber optic Fabry-Perot pressure sensor with temperature compensation[J]. Chinese Optics, 2025, 18(5): 1255-1265.
王昊星，刘佳，王海洋，等. 具有温度补偿的金属膜片式光纤法珀压力传感器(英文)[J]. 中国光学，2025，18(5)：1255-1265.

[21] Liu Jia, Zhang Lei, Wang Ziyue, et al. Extreme Dual-Parameter Optical Fiber Sensor Composed of MgO Fabry-Perot Composite Cavities for Simultaneous Measurement of Temperature and Pressure[J]. Applied Sciences, 2025, 15(16): 8891.

[22] FADEEV K M, LARIONOV D D, ZHIKINA L A, et al. A fiber-optic sensor for simultaneous temperature and pressure measurements based on a Fabry – Perot interferometer and a fiber Bragg grating[J]. Instruments and Experimental Techniques, 2020, 63(4): 543-546.

[23] DI GIOVANNI M. Flat and corrugated diaphragm design handbook[M]. Routledge, 2017.

[24] SUN Yan, FENG Ganhua, GEORGIOU G, et al. Center embossed diaphragm design guidelines and Fabry-Perot diaphragm fiber optic sensor[J]. Microelectronics journal, 2008, 39(5): 711-716.

[25] LI Wenhao, JIA Pinggang, WANG Jun, et al. High Sensitivity Micro Fiber Fabry Perot Pressure Sensor Based on Silicon MEMS Technology[J]. Acta Photonica Sinica, 2024, 53(5): 0553110.
李文豪，贾平岗，王军，等. 基于硅MEMS技术的高灵敏度微型光纤法布里-珀罗压力传感器[J]. 光子学报，2024，53(5)：0553110.

Research on Fiber Optic Fabry-Perot Temperature and Pressure Dual Parameter Sensor Based on MEMS Technology

LIU Guoke, WANG Jun, DAI Yunteng, LIU Jia, REN Qianyu, JIA Pinggang
(*State Key Laboratory of Widegap Semiconductor Optoelectronic Materials and Technologies*, *Northern University of China*, *Taiyuan* 030051, *China*)

Abstract: To address the technological bottlenecks faced by pressure measurement in high-temperature environments in aerospace, energy and chemical industries, such as severe temperature cross-sensitivity, insufficient stability of traditional electrical sensors, and the difficulty for existing optical sensors to combine high-precision measurement with mass production, this paper proposes a new solution to develop a temperature-pressure dual-parameter fiber optic Fabry-Perot sensor. By designing a silicon-based sensitive diaphragm with a central boss structure, the silicon sensing element enables simultaneous, integrated measurement of both temperature and pressure at the same point while achieving temperature decoupling. This design effectively suppresses cross-interference between temperature and pressure, enhances the accuracy of pressure measurement in complex environments and holds considerable potential for engineering applications. This work combines the fiber-optic Fabry-Perot interferometric principle with MEMS technology to design a monocrystalline silicon diaphragm featuring an internal central boss as the core sensing element. This element integrates a pressure-sensing cavity (FP1) and a temperature-sensing cavity (FP2) on the same diaphragm. The FP1 cavity is formed between the fiber end-face and the inner surface of the diaphragm, and its cavity length varies with external pressure. The FP2 cavity, on the other hand, is defined by the entire thickness of the silicon boss, making it more sensitive to temperature variations through the thermal expansion of silicon. With this monolithic design, no additional temperature reference element is required, and dual-parameter measurement is achieved at the same physical location, fundamentally avoiding the measurement error caused by spatial separation of temperature and pressure sensing elements, which is common in conventional approaches. Based on small-deflection theory, the relationship between the central deflection of the diaphragm and the uniformly distributed pressure is analyzed. Finite element simulations are performed to optimize the geometric dimensions of the diaphragm structure, and the beneficial effect of the boss structure on improving the flatness of the central region under pressure is investigated, thereby reducing the demodulation difficulty caused by arc-shaped deformation of the interference surface. In terms of fabrication, standard MEMS processes including uniform photoresist, photolithography, development, and etching are employed for batch production of the sensitive diaphragm. After fabrication, the four-inch silicon wafer is anodically bonded to a borosilicate glass substrate, ensuring hermeticity at high temperatures. The bonded wafer is then diced into individual 4 mm × 4 mm sensing elements. CO_2 laser welding is adopted to achieve all-solid-state, adhesive-free integration of the sensing element with the optical fiber, further reducing the risk of gas leakage at high temperatures caused by mismatched thermal expansion of materials. A temperature-pressure composite test platform is established to evaluate the overall performance of the integrated sensor. First, static pressure tests are performed from atmospheric pressure up to 500 kPa in steps of 100 kPa to characterize the linearity, sensitivity, hysteresis, and repeatability. Subsequently, temperature-pressure composite tests are conducted at temperature points of 22 °C, 50 °C, 100 °C, 150 °C, 200 °C, 250 °C, 300 °C, and 350 °C. During the experiments, an interrogator is used to acquire the interference spectrum in real time, and a cross-correlation demodulation algorithm is applied to accurately extract the cavity lengths of FP1 and FP2 from the composite interference spectrum. Subsequently, a temperature measurement model based on the FP2 cavity length is built, together with a compensation relationship that accounts for the temperature-induced drift of the initial cavity length L_0 and the pressure sensitivity. Finally, real-time temperature decoupling of the pressure signal is achieved. The comprehensive performance of the sensor is experimentally verified over the ranges of 22 °C to 350 °C and 0 to 500 kPa. Static pressure characterization shows that the sensor exhibits excellent static characteristics: a nonlinearity error of 0.17% F.S, a hysteresis error of 0.62% F.S, a repeatability error of 0.72% F.S, and a pressure sensitivity of 0.83 nm/kPa, which is in good agreement with the design value of 0.85 nm/kPa. High-temperature tests demonstrate that the sensor can measure temperature autonomously. At 350 °C, the decoupled temperature is 349.26 °C, with a deviation of only 0.74 °C, corresponding to a temperature measurement accuracy of 0.21% F.S. Moreover, an increase in pressure sensitivity with rising temperature is observed, and a cubic polynomial relationship between sensitivity and temperature is established. After applying temperature compensation using the decoupling algorithm, the pressure measurement accuracy at high temperatures is significantly improved. Taking 350 °

C as an example, the maximum measurement error is reduced to less than 1.17% F.S. The experimental data confirm that the proposed boss-type diaphragm structure can effectively separate temperature and pressure induced signals, achieve co-located dual-parameter measurement, and thereby enhance pressure measurement accuracy. This paper presents a MEMS-based fiber-optic F-P dual-parameter sensor for simultaneous temperature and pressure measurement. Through the innovative boss diaphragm design, the sensor achieves co-located dual-parameter measurement based on the deformation of a monolithic silicon sensing diaphragm under composite environments, without introducing any additional temperature sensing elements. Experimental results demonstrate that the sensor's built-in temperature sensing and decoupling mechanism can effectively mitigate the temperature-pressure cross-sensitivity issue in high-temperature pressure measurement. This work provides a new technical solution for accurate pressure monitoring in harsh high-temperature environments such as aero-engine hot-section components and chemical processes, holding significant application value and broad prospects for industrial adoption.

Key words: Fiber optics sensors; Fabry-Perot; MEMS; Temperature-Pressure measurement; High temperature

OCIS Codes: 060.2370; 120.2230; 120.5475; 120.6780

CSTR: 32255.14.gzxb20265507.0706002

Foundation item: National Natural Science Foundation of China (52505617)